

# Supplementary information

## Graphene under extreme electromagnetic field: energetic ion acceleration by direct irradiation of ultra intense laser on few layer suspended graphene

### THOMSON PARABOLA SPECTROMETER

Thomson parabola spectrometer (TPS) is one of the most widely used diagnostics for laser driven ion acceleration. By applying electric ( $\vec{E}$ ) and magnetic ( $\vec{B}$ ) fields TPS allows us to obtain energy spectra for ions with different charge-to-mass ratio. Ions with the same charge-to-mass ratio but different energies form a parabola on a detector plane as schematically shown in Supplementary Figure 1 (a). Assuming an accelerated ion going along the  $z$ -axis with the velocity of  $\vec{v}$ , and  $\vec{E}$  and  $\vec{B}$  fields to be in the  $x$ -axis, the ion trajectory deviates from the dashed line corresponding to a neutral particle or infinite energy charged particle trajectories due to  $q\vec{E}$  and  $q\vec{v} \times \vec{B}$  in  $x$  and  $y$  directions, respectively. By neglecting the fringing fields, the displacement in each direction for non-relativistic ions can be written as

$$x_D = \frac{qEL}{mv^2} \left( \frac{L}{2} + D \right), \quad y_D = \frac{qBL}{mv} \left( \frac{L}{2} + D \right), \quad (1)$$

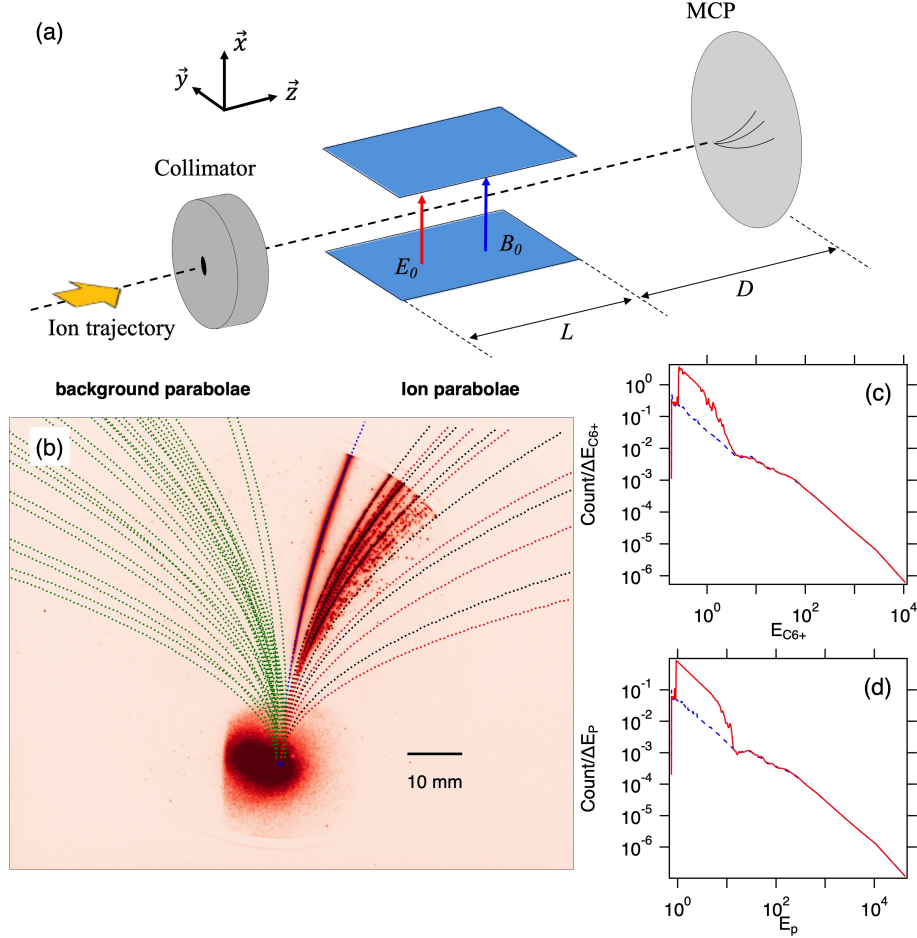
where  $q$  and  $m$  are ion charge and mass,  $c$  is the speed of light,  $L$  and  $D$  defined as in Supplementary Figure 1 (a). Eliminating  $v$  from Eq. (1), one obtains the parabolic formula on the detector as

$$y_D^2 = \alpha \frac{q}{m} x_D, \quad (2)$$

where  $\alpha \equiv B^2 L(L/2 + D)/E$ .

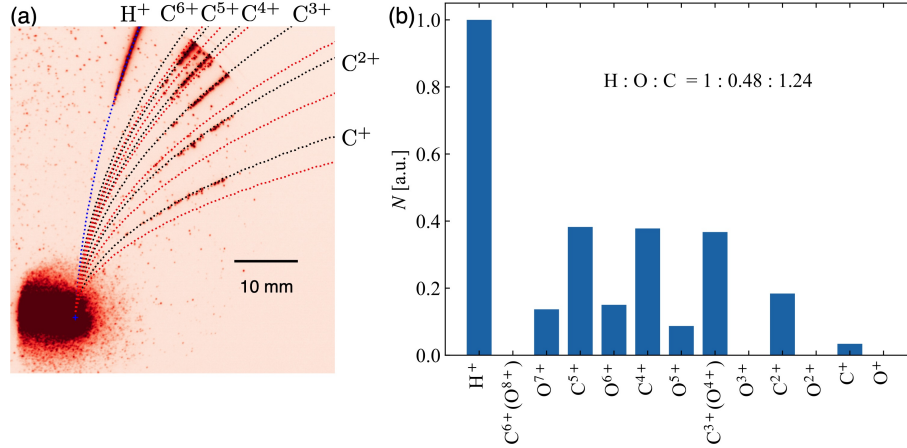
Supplementary Figure 1 (b) shows the signal from the MCP taken by CCD camera with a commercial lens, which is the same data as in Fig. 2 (a). We fit the proton parabola with Eq. (2) with least squares fitting method using  $\alpha$  and the rotation of the image coming from the slight uncertainty of TPS and camera alignment as free parameters. Using the same fit parameters with different  $q/m$  all the other parabolae from carbons and oxygens are well fitted as shown in Supplementary Figure 1 (b)

In order to subtract the background signals, we consider imaginary particles moving oppositely by electric field ( $\vec{E}$ ) but correctly with magnetic field ( $\vec{B}$ ) as shown in Supplementary Figure 1 (b). Since the background signals come from the  $x$ - and  $\gamma$ -rays and also



Supplementary Figure 1. (a) Schematic drawing of Thomson parabola spectrometer. The nominal parameters used in the experiment are  $B = 0.165$  T,  $E = 0.444$  kV/mm,  $L = 100$  mm, and  $D = 497$  mm. The diameter of the MCP is 75 mm, and the collimator ( $\phi = 300\mu\text{m}$ ) is placed  $\sim 1.5$  m away from the target. (b) Thomson parabola image with 8-layer LSG, which is the same data as in Fig. 2. We consider imaginary particles in order to subtract background from the ion side signals. (c) and (d) The carbon 6+ and proton spectra are shown with the background taken from the symmetric parabolae, respectively.

from neutral particles those recombined with electrons on the way to the detector, they are not sensitive to  $\vec{E}$  and  $\vec{B}$  fields. Since the TPS has mechanical structure symmetric in terms of a plane parallel to the  $y$  axis and containing the dashed line in Supplementary Figure 1 (a), we consider the parabolae corresponding to the imaginary particles as in Supplementary Figure 1 (b). For the background parabolae we take a finite width as shown in Supplementary Figure 1 (b) to suppress the spiky noise, which is not very clear in Sup-



Supplementary Figure 2. (a) Thomson parabola image with 4-layer LSG. The dotted lines show the parabolae corresponding to H<sup>+</sup> (blue), C<sup>1+</sup>–C<sup>6+</sup> (black), and O<sup>1+</sup>–O<sup>8+</sup> (red), where O<sup>8+(4+)</sup> lines on the same line as C<sup>6+(3+)</sup>. (b) The composition ratio of LSG generated ions normalized to proton population.

plementary Figure 1 (b), but can be seen in Supplementary Figure 2 (a). Supplementary Figure 1 (c) and (d) correspond to the carbon 6+ and proton spectra together with the symmetric parabolae, respectively. The ion and background signals agree very well at high energies, allowing us to estimate the maximum measurable energies of ions.

## COMPOSITION

In order to confirm the composition of the graphene and contamination, we have conducted a calibration experiment with J-KAREN-P at low energy with defocusing but strong enough to generate ion beams. A 4-layer LSG is irradiated with a short pulse laser (energy 4 J, pulse duration 30 fs, wavelength 800 nm, spot size is defocused to 126  $\mu\text{m}$  in order to make the intensity  $\sim 1 \times 10^{17} \text{ Wcm}^{-2}$ ), and the generated ions are measured with TPS. Supplementary Figure 2 (a) shows the raw data from TPS. The bright circular feature corresponds to the x-rays,  $\gamma$ -rays, and neutral particles, and the dark dot in the bright feature corresponds to the zero displacement, i.e., corresponding to ions with infinite energy, determined with the vacuum shot. As shown in Supplementary Fig. 2 (a), not only carbon ions but also oxygen ions are generated from the LSG, but carbons are clearly much more than oxygens. With the low energy shot we can easily confirm the carbon and oxygen lines

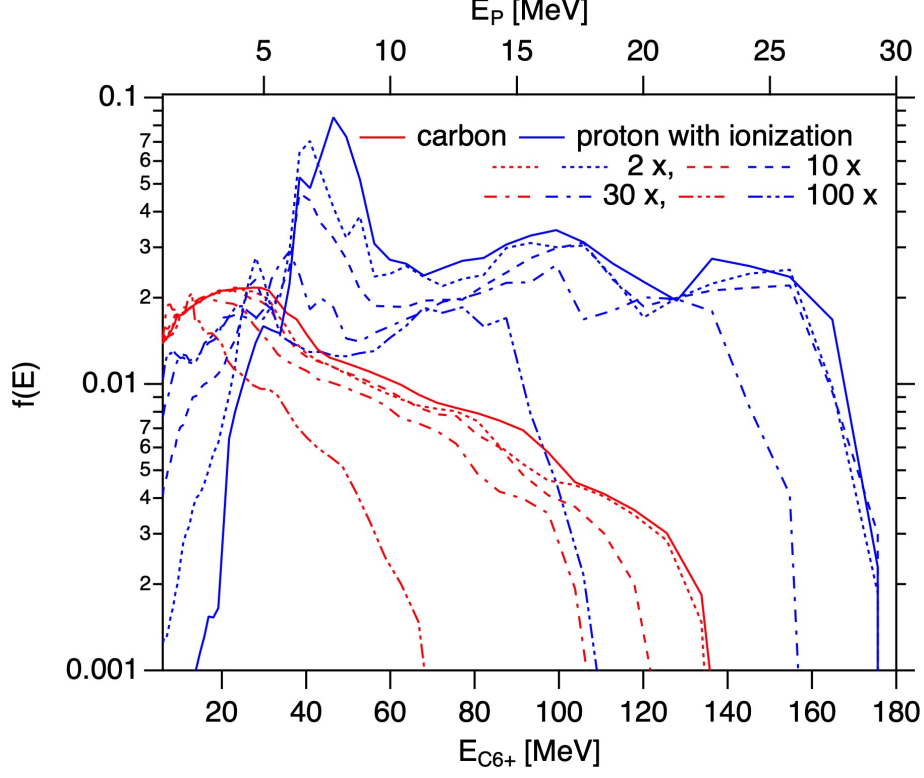
without saturation and overlapping of signals. There is no low Z carbon/oxygen with the high energy shots as shown in Fig. 2 (a) and the parabolae at high energies overlap each other making it difficult to estimate the composition.

Supplementary Figure 2 (b) shows the composition ratio obtained from Supplementary Figure 2 (a). We calculate the distribution function by converting the displacement to the ion energies, and then, integrate the distribution functions along the parabolae. We define the background with the population corresponding to  $C^{6+}+O^{8+}$  to be zero. After subtracting the background we normalize all the populations to the proton population. From Supplementary Fig. 2 (b) it is evident that the oxygen ions are much less than carbon ions. We sum up carbon and oxygen separately and using the summed ratio we divide the  $C^{3+}$  and  $O^{4+}$  into carbon and oxygen, and finally by summing up all the charge states for each ion species we obtained the composition ratio, proton : oxygen : carbon = 1: 0.48 : 1.24. Note that the integral domains for energies are limited by the size of detector, and thus, there are particles outside of our integral domains. Nevertheless, the proton to oxygen is close to two to one, indicating the contamination comes from water. The composition of carbon ( $H_2O$ ) is 72% (28%). As we mention, there is no chemical bond in the Raman spectra other than graphene, and thus, the contamination should exist as “particles”.

## PARTICLE-IN-CELL SIMULATIONS

We perform 1D and 2D PIC simulations for the J-KAREN-P experiment using an open simulation code EPOCH [4]. We fix the laser parameters based on the experimental conditions, and linearly polarized Gaussian beam in simulation plane. We consider the target ionization with the laser electric field via barrier suppression, tunneling, and multi photon ionization processes with a standard option of EPOCH. Ionization thresholds of atoms are cited from Atomic Spectra Database[5]

The areal density of graphene is  $\sigma = 3.82 \times 10^{15} \text{ cm}^{-2}$ . Our LSG thickness is 1 nm / layer, and thus, the LSG volume density is  $3.82 \times 10^{22} \text{ cm}^{-3}$  and the electron density is 6 times more when fully stripped. As discussed above, the composition of the target is proton : oxygen : carbon = 1: 0.48 : 1.24, and that the total electron number, which is essential for the laser-matter interaction, is  $(1+0.48 \times 8+1.24 \times 6)/(1.24 \times 6) = 12.28/7.44 = 1.65$  times more than that from graphene. We fix the electron density as  $n_e = 1.65 \times 6 \times 3.82 \times 10^{22} = 3.78 \times 10^{23}$



Supplementary Figure 3. The energy distribution functions of carbons (red) and protons (blue) with pre-ionized expanded targets due to the effects of pre-pulse and pedestal of laser. For comparison we also plot the case with ionization with laser (solid lines), which is the same as in Fig. 4 (b). We consider the expansions of target thickness by factors 2 (dotted lines), 10 (dashed lines), 30 (dash-dotted lines), and 100 (dash-two-dots lines) and reduce the number density by the same factors. We set the top axis to be 1/6 of bottom axis.

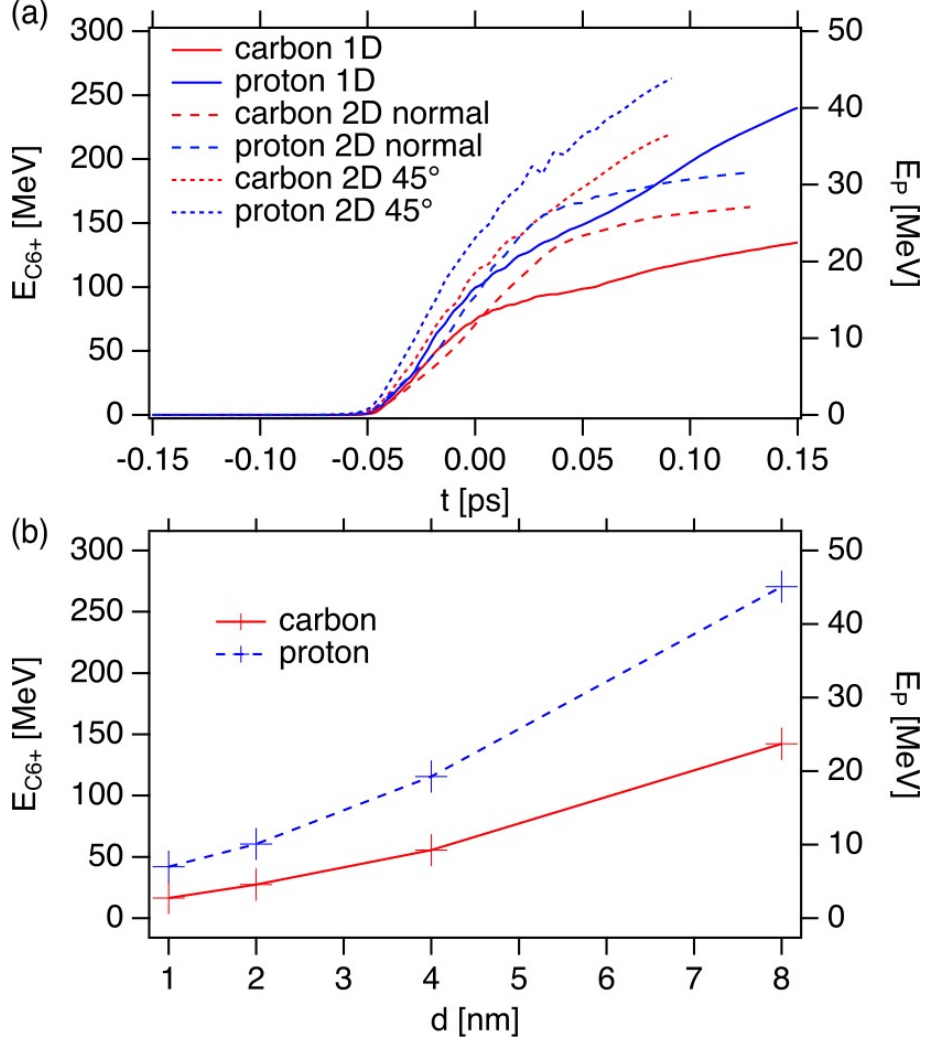
$\text{cm}^{-3}$ . Here we consider all the heavier ions are carbon for simplicity; the proton ratio is set to be  $1/(1 + 11.28/6) \sim 0.35$  of all atoms. We define carbon and proton densities as  $n_C = 0.65 \times n_e / (0.65 \times 6 + 0.35)$  and  $n_P = 0.35 \times n_e / 4.25$ , respectively. Note that we do not consider the graphene structure in the simulations.

The numerical parameters used in the runs are settled after the massive conversion tests as; for 1D simulations the grid size is  $\Delta x = 0.1, 0.2, 0.4$ , and  $0.8$  for 1, 2, 4, and 8-layer LSG respectively, the number of particles per cell is 1000, and the number of grids is  $N_x = 550000, 300000, 150000$ , and  $75000$  for 1, 2, 4, and 8-layer LSG corresponding to the system size of  $L_x = 55\mu\text{m}$  for 1-layer LSG and  $60\mu\text{m}$  for 2–8 layer LSG. For 2D simulations with the normal incidence of laser to the target,  $\Delta x = 1.6\text{nm}$  where the laser propagates along the  $x$

axis,  $\Delta y = 16$  nm, and  $(N_x, N_y) = (37500, 1875)$ , corresponding to  $(L_x, L_y) = (60, 30)\mu\text{m}$ . For the 45 degrees incidence, which is shown in Fig. 4,  $\Delta x = \Delta y = 1.6$  nm, and  $(N_x, N_y) = (12500, 12500)$ , corresponding to  $(L_x, L_y) = (20, 20)\mu\text{m}$ , which is much more costly than the normal incidence case. Since the target is placed 45 degrees from the laser propagation axis, which is also along the  $x$  axis, we have to resolve the target in the  $y$  direction as well as the  $x$  direction.

The results of 2D run with the 45 degrees incidence are shown in Fig. 4. The numerically obtained ion energies are higher than that of experiment, indicating that the target is melted prior to the main laser arrival due to the pre-pulse and pedestal. We consider the effects of pre-pulse and pedestal by using pre-ionized expanded targets. Keeping the total number of physical particles constant, we run the pre-ionized expanded targets, where the thickness is 2, 10, 30, 100 times thicker than the run for Fig. 4 (a), with the reduced densities by the same factors. We also reduce the numerical resolution by multiplying the same factor to  $\Delta x$  and  $\Delta y$ , until it becomes larger than  $\lambda/32$ , where  $\lambda$  is the laser wavelength. This allows us to save tremendous amount of computation time and resources. Supplementary Figure 3 (a) shows the distribution functions of carbons (red) and protons (blue) where the top axes scale 1/6 of bottom axis. We also show the results with ionization processes for reference, which is the same as the solid lines in Fig. 4 (b). From these results we can conclude that the ionization is not essential; the twice thicker target with half density (dotted lines) results in almost same distribution functions with ionization (solid lines). Especially for protons 10 times expansion (blue dashed line) shows mere difference from the ionization case (blue solid line). As the expansion factor become larger, the carbon and proton maximum energies become smaller. Using 100 times thicker target with  $0.01n_e$ , the carbon and proton energies become comparable to the experimental results. Note that the density is still higher than the critical density.

Supplementary Figure 4 (a) shows the time evolution of the maximum carbon and proton energies in the runs. The left axis is scaled as it is 6 times larger than the right axis. In all the runs, protons are accelerated comparable to or more efficiently than the 1/6 of carbon energies, as the lighter particles are more efficiently accelerated. The maximum ion energies in 1D simulations are larger than those in 2D simulations in general, since the transverse directions in 1D simulations are homogeneous, and also potential field drops in space more quickly in 2D. This is true for protons with normal incidence. While in the 2D normal



Supplementary Figure 4. (a) The time evolution of maximum carbon ( $E_{C6+}$ , red) and proton energies ( $E_p$ , blue) with 1D (solid lines) and 2D PIC simulations. For 2D simulations the dashed (dotted) lines correspond to the normal (45 degrees) incidence of the laser to the target. For comparison purpose, we also calculated the higher density cases as we used in Vulcan simulations; the dashed-dotted (dashed-two dotted) lines correspond to the 1D (2D normal) high density run. The time 0 corresponds to the laser peak arrival at the target. (b) The maximum ion energies are plotted in terms of target thickness from the 1D simulations.

incidence simulations the proton and carbon maximum energies are almost saturated, in the 1D runs they are still increasing in Supplementary Figure 4 (a).

By comparing the incident angle, the 45 degrees incidence results in higher maximum energies than those in the normal incidence in Supplementary Figure 4 (a). This can be the

fact that the effective target thickness is  $\sqrt{2}$  times thicker in 45 degrees incidence than that of the normal incidence, since the target is still too thin for the J-KAREN-P laser as shown in Fig. 4 (b). While the normal incidence is consider to be better for the RPA [6–8], it is still open for the extremely thin target regime with LSG.

Figure 4 (b) shows the maximum ion energies from 1D simulations plotted against the target thickness. Since the 2D simulations are much more costly than the 1D simulations, we use only 1D simulations, and we simulate longer time in the 1D simulations  $\sim 2$  ps from the peak arrival. At the single figure nm thickness the maximum ion energies increase as the number of LSG layers; as mentioned above the target thickness is still too thin for extremely intense laser with  $\sim 10^{22}$  Wcm $^{-2}$ .

- 
- [1] H. Kiriya, A. S. Pirozhkov, M. Nishiuchi, Y. Fukuda, K. Ogura, A. Sagisaka, Y. Miyasaka, M. Mori, H. Sakaki, N. P. Dover, K. Kondo, J. K. Koga, T. Z. Esirkepov, M. Kando, and K. Kondo, *Optics Letters* **43**, 2595 (2018).
  - [2] S.-E. Zhu, S. Yuan, and G. C. A. M. Janssen, *EPL (Europhysics Letters)* **108**, 17007 (2014).
  - [3] S. Pang, Y. Hernandez, X. Feng, and K. Müllen, *Advanced Materials* **23**, 2779 (2011).
  - [4] T. D. Arber, K. Bennett, C. S. Brady, A. Lawrence-Douglas, M. G. Ramsay, N. J. Sircombe, P. Gillies, R. G. Evans, H. Schmitz, A. R. Bell, and C. P. Ridgers, *Plasma Physics and Controlled Fusion* **57**, 113001 (2015).
  - [5] “NIST: Atomic Spectra Database - Ionization Energies Form,” <https://physics.nist.gov/PhysRefData/ASD/ionEnergy.html>.
  - [6] T. Esirkepov, M. Borghesi, S. V. Bulanov, G. Mourou, and T. Tajima, *Physical Review Letters* **92**, 175003 (2004).
  - [7] A. P. L. Robinson, M. Zepf, S. Kar, R. G. Evans, and C. Bellei, *New Journal of Physics* **10**, 013021 (2008).
  - [8] A. Macchi, S. Veghini, and F. Pegoraro, *Phys. Rev. Lett.* **103**, 085003 (2009).